DIRECT NUMERICAL SIMULATION OF PARTICLE MIXING IN DISPERSED GAS-LIQUID-SOLID FLOWS USING A COMBINED VOLUME OF FLUID AND DISCRETE PARTICLE APPROACH

Niels G. DEEN, Martin VAN SINT ANNALAND and J.A.M. KUIPERS

University of Twente, Fac. of Science and Technology, PO Box 217, 7500 AE Enschede, THE NETHERLANDS

ABSTRACT

In this paper a hybrid model is presented for the numerical simulation of gas-liquid-solid flows using a combined Volume Of Fluid (VOF) and Discrete Particle (DP) approach applied for respectively dispersed gas bubbles and solid particles present in the continuous liquid phase. The hard sphere DP model, originally developed by Hoomans et al. (1996) for dense gas-solid systems, has been extended to account for all additional forces acting on particles suspended in a viscous liquid and has been combined with the VOF model presented recently by van Sint Annaland et al. (2005) for complex free surface flows. In this paper the physical foundation of the combined VOF-DP model will be presented together with illustrative computational results highlighting the capabilities of this hybrid model. The effect of bubble-induced particle mixing has been studied focusing on the effect of the volumetric particle concentration. In addition particle mixing was studied in systems with coalescing bubbles.

NOMENCLATURE

a	Computational domain in x-direction (m)
C_d	Drag coeff. for an isolated spherical particle (-)
C_L	Lift coefficient (-)
C_{VM}	Virtual mass coefficient (-)
d	Plane constant for interface segment cutting through Eulerian cell (-)
d_e	Equivalent bubble diameter (m)
d_p	Particle diameter (-)
D	Distribution or smoothening function (-)
Eo	Eötvös number (-)
F	Fractional amount of liquid (-)
$\tilde{F}$	Smoothed colour function (-)
F_σ	Volumetric surface tension force (N/m³)
h	Width of the computational stencil for the smoothening function (m) Measure for Eulerian grid size (m)
L	Length of square duct (m)
M	Morton number (-)
m_p	Particle mass (kg)
N_p	Number of suspended solid particles (-)
n_i	i^{th} component of the unit normal vector (-)
p	Pressure (N/m²)
R	Bubble radius (m)
Re	Reynolds number (-)
t	Time (s)
U_0	Superficial velocity (m/s)
V_b	Bubble volume (m³)
V_p	Particle volume (m³)
V_s	Initial suspension volume (m³)
v_∞	Terminal bubble rise velocity (m/s)
X_d	Dimensionless volume of drift zone (-)
x_i	i^{th} co-ordinate direction (m)
x	x co-ordinate (m)
y	y-co-ordinate (m)
z	z-co-ordinate (m)

Greek letters

β_p	Effective fluid-particle friction coefficient (kg/(m³.s))
ϕ	Dimensionless liquid velocity (-)
ε_f	Liquid phase volume fraction (-)
κ	Curvature (m⁻¹)
μ	Dynamic viscosity (kg/(m.s))
ρ	Density (kg/m³)
$\Delta\rho$	Density difference (kg/m³)
Δx_i	Grid spacing in i^{th} co-ordinate direction (m)
σ	Surface tension (N/m)
ξ_i	Dimensionless i^{th} co-ordinate direction

Vectors

$\overline{F}_g$	Gravity force (N)
$\overline{F}_p$	Pressure force (N)
$\overline{F}_d$	Drag force (N)
$\overline{F}_L$	Lift force (N)
$\overline{F}_{VM}$	Virtual mass force (N)
$\overline{F}_\sigma$	Volumetric surface tension force (N/m³)
$\overline{F}_{f \to s}$	Volumetric force due to fluid-solid coupling (N/m³)
$\overline{g}$	Gravitational acceleration (m/s²)
$\overline{m}$	Normal vector
$\overline{n}$	Unit normal vector
$\overline{u}$	Fluid velocity (m/s)
$\overline{v}$	Particle velocity (m/s)

Subscripts and superscripts

g	Gas phase
l	Liquid phase
p	Particle phase
x	x-direction
y	y-direction
z	z-direction

Operators

$\partial / \partial t$ Partial time derivative (s^{-1})

D / Dt Substantial derivative (s^{-1})

∇ Gradient operator (m^{-1})

$\nabla \cdot$ Divergence operator (m^{-1})

T Transpose of a tensor

$\otimes$ Cross vector product

INTRODUCTION

Multiphase systems are frequently encountered in a variety of industrial processes involving a.o. coating, granulation, drying and synthesis of fuels (Fischer Tropsch) and base chemicals. The hydrodynamics of multiphase systems is dictated by the motion of the individual phases and the complex mutual interactions and as a direct consequence thereof CFD-based modelling of these systems has proven notoriously difficult. In literature both the Eulerian approach (Torvik and Svendsen, 1990; Mitra-Majumdar et al., 1997) and Lagrangian approach (Bourloutski and Sommerfeld, 2002) have been adopted to study gas-liquid-solid three-phase flows. Although these computational methods are in principle well-suited to simulate the large-scale flow behaviour of slurry bubble columns and three-phase fluidized beds (i.e. the time-averaged circulation pattern and spatial gas holdup distribution), problems arise related to the representation of the interactions between the individual phases leading to considerable closure problems.

To overcome this problem detailed microscopic models can be used to generate closure laws which are needed in coarse-grained simulation models which are used to describe the macroscopic behaviour and as a practical consequence thereof do not resolve all the relevant length and time scales. This multi-scale modelling approach has been used by the authors previously for dense gas-solid flows (van der Hoef et al., 2004) and for dispersed gas-liquid two-phase flows (van Sint Annaland et al., 2003 and Deen et al., 2004a, 2004b) and can in principle be used for other types of multiphase flow as well. Our model is based on a combined Volume Of Fluid (VOF) and Discrete Particle (DP) approach applied for respectively dispersed gas bubbles and solid particles present in the continuous liquid phase.

Volume Of Fluid (VOF) methods (Hirt and Nichols, 1981; Youngs, 1982; Rudman, 1997, 1998; Rider and Kothe, 1998; Scardovelli and Zaleski, 1999; Popinet and Zaleski, 1999; Bussman et al., 1999) employ a colour function F(x,y,z,t) that indicates the fractional amount of fluid present at a certain position (x,y,z) at time t. The evolution equation for F is usually solved using special advection schemes (such as geometrical advection, a pseudo-Lagragian technique), in order to minimize numerical diffusion. In addition to the value of the colour function the interface orientation needs to be determined, which follows from the gradient of the colour function. Roughly two important classes of VOF methods can be distinguished with respect to the representation of the interface, namely Simple Line Interface Calculation (SLIC) and Piecewise Linear Interface Calculation (PLIC). Earlier work is generally typified by the SLIC algorithm due to Noh and Woodward (1976) and the Donor-Acceptor algorithm published by Hirt and Nichols (1981). Modern VOF techniques include the PLIC method due to Youngs (1982). The accuracy and capabilities of the modern PLIC VOF algorithms greatly exceeds that of the older VOF algorithms such as the Hirt and Nichols VOF method (Rudman, 1997). A drawback of VOF methods is the so-called artificial (or numerical) coalescence of gas bubbles which occurs when their mutual distances is less than the size of the computational cell.

Discrete Particles (DP) methods employ particle tracking taking into account i) all relevant external forces (gravity, pressure, drag, lift and virtual mass forces) acting on the particles and ii) collisions between particles and confining walls. Finally, two-way coupling, which becomes important at high solids volume fraction, is also taken into account. In this study the hard sphere DP model, originally developed by Hoomans et al. (1996) for gas-solid systems (also see Hoomans, 2000), has been extended to account for all additional forces acting on particles suspended in a viscous liquid and has been combined with the VOF model presented recently by van Sint Annaland et al. (2005). The direct numerical simulation has been pioneered by Fan and co-workers (Li et al., 1999, 2000, 2001; Zhang et al., 2000a, 2000b) who used a two-dimensional model based on the VOF method to track the bubble interface.

The organisation of this paper is as follows: first the description of the model is given followed by a description of the numerical solution method. Subsequently the results are presented and discussed and finally the conclusions are presented.

MODEL DESCRIPTION

Our model consists of two major sub-models, the model dealing with the motion of the gas bubbles in the continuous phase (consisting of liquid and suspended solid particles) and the DP model dealing with the motion of the suspended particles taking into account the action of external forces and non-ideal particle-particle and particle-wall collisions. First the VOF model is briefly described followed by a brief description of the DP model.

Volume of fluid model

The governing conservation equations for unsteady, Newtonian, multi-fluid flows are given by the following expressions:

$$\frac{\partial \varepsilon_f}{\partial t} + (\nabla \cdot \varepsilon_f \overline{u}) = 0 \tag{1}$$

$$\rho[\frac{\partial}{\partial t}(\varepsilon_f \overline{u}) + (\nabla \cdot \varepsilon_f \overline{u}\overline{u})] = -\varepsilon_f \nabla p + \rho \overline{g} - \overline{F}_{f \to s}$$
$$+ (\nabla \cdot \varepsilon_f \mu[(\nabla \overline{u}) + (\nabla \overline{u})^T]) + \overline{F}_\sigma \tag{2}$$

The source terms $\overline{F}_\sigma$ and $\overline{F}_{f \to s}$ account respectively for the forces due to surface tension and two-way coupling due to the presence of the suspended solid particles. Furthermore ε_f represents the volume fraction of the continuous liquid phase. The mixture density ρ and viscosity μ are evaluated from the local distribution of the phase indicator or colour function function F which is governed for by:

$$\frac{DF}{Dt} = \frac{\partial F}{\partial t} + (\overline{u} \cdot \nabla F) = 0 \tag{3}$$

expressing that the interface property is advected with the local fluid velocity. For the local average density ρ linear weighing of the densities of the liquid (l) and gas phase (g) is used:

$$\rho = F\rho_l + (1-F)\rho_g \tag{4}$$

Similarly, the local average dynamic viscosity can also be obtained via linear averaging of the dynamic viscosities of the liquid and gas phase. As an alternative, more fundamental approach recently proposed by Prosperetti (2001), the local average viscosity can be calculated via harmonic averaging of the kinematic viscosities of the involved phases according to the following expression:

$$\frac{\rho}{\mu} = F\frac{\rho_l}{\mu_l} + (1-F)\frac{\rho_g}{\mu_g} \tag{5}$$

In all computations reported in this paper Eq. (5) was used to compute the local average viscosity. The volumetric surface tension force appearing in the momentum Eq. (2) acts only in the vicinity of the interface

Discrete particle model

The motion of the suspended solid particles is given by the Newton's second law given by the following expression which accounts for the action of gravity, far-field pressure, drag, lift and added mass forces.

$$\begin{aligned}
\frac{d}{dt}(m_p\overline{v}) &= \overline{F}_g + \overline{F}_p + \overline{F}_d + \overline{F}_L + \overline{F}_{VM} \\
&= m_p\overline{g} - V_p\nabla p + \frac{V_p\beta_p}{(1-\varepsilon_f)}(\overline{u}-\overline{v}) \\
&\quad - C_L V_p\rho_l(\overline{v}-\overline{u})\times(\nabla\times\overline{u}) \\
&\quad - \rho_l V_p C_{VM}[\frac{D}{Dt}(\overline{v}-\overline{u})+(\overline{v}-\overline{u})\cdot(\nabla\overline{u})]
\end{aligned} \tag{6}$$

This equation is similar to the one used by Delnoij et al. (1997) in their discrete bubble model for dispersed gas-liquid two-phase flow. Since the size of the particles typically is (much) smaller than the size of the computational grid required for capturing the bubble dynamics, a closure equation is required for the effective drag (friction) acting on the particles. Following Hoomans et al. (1996) the friction between the continuous liquid phase and the suspended solid particles is given by the Ergun equation in the dense regime ($\varepsilon_f < 0.8$) and the Wen and Yu equation in the dilute regime ($\varepsilon_f > 0.8$) respectively given by ($\varepsilon_f < 0.8$):

$$\beta_p = 150\frac{(1-\varepsilon_f)^2}{\varepsilon_f}\frac{\mu_l}{(d_p)^2} + 1.75(1-\varepsilon_f)\frac{\rho_l}{d_p}|\overline{u}-\overline{v}| \tag{7a}$$

and ($\varepsilon_f > 0.8$):

$$\beta_p = \frac{3}{4}C_d\frac{\varepsilon_f(1-\varepsilon_f)}{d_p}\rho_l|\overline{u}-\overline{v}|(\varepsilon_f)^{-2.65} \tag{7b}$$

where the drag coefficient C_d follows well-known equations for drag coefficients for spheres whereas $C_{VM} = 0.5$ and $C_L = 0.5$ was assumed. Alternatively drag closure equations obtained from LB models can be used for the effective drag closure (van der Hoef et al., 2004, 2005). For the (possible) non-ideal particle-particle and particle-wall collisions we use a three parameter model accounting for normal and tangential restitution and friction. The associated collision parameters will respectively be denoted by e_n, e_t and μ.

NUMERICAL SOLUTION METHOD

Computation of the flow field

The Navier-Stokes equations can be solved with a standard finite volume technique on a staggered rectangular three-dimensional grid using a two-step projection-correction method with an implicit treatment of the pressure gradient and explicit treatment of the convection and diffusion terms. A second order flux delimited Barton-scheme (Centrella and Wilson, 1984) is used for the discretisation of the convection terms and standard second order central finite differences for the diffusion terms. We use a robust and very efficient Incomplete Cholesky Conjugate Gradient (ICCG) algorithm to solve the Pressure Poisson Equation (PPE).

Computation of the surface force

In the CSF model (Brackbill et al., 1992) the surface tension force acts via a source term $\overline{f}_\sigma$ in the momentum equation which only acts in the vicinity of the interface. The expression for $\overline{f}_\sigma$ is given by

$$\overline{f}_\sigma = 2F\sigma\kappa\overline{m} \tag{8}$$

where the expression for the curvature is obtained from the divergence of the unit normal vector to the interface:

$$\kappa = -(\nabla\cdot\overline{n}) = \frac{1}{|\overline{m}|}\left[\frac{\overline{m}}{|\overline{m}|}\cdot\nabla|\overline{m}| - (\nabla\cdot\overline{m})\right] \tag{9}$$

The normal to the interface is computed from the gradient of the smoothed colour function. The smoothing technique used in this paper will be discussed later.

Solution of the F-advection equation

The integration of the hyperbolic F-advection equation is the most critical part of the VOF model and is based on geometrical advection which can be viewed as a pseudo-Lagrangian advection step. The advantage of the geometrical advection is given by the fact that a very sharp interface is maintained during the simulations. First for each Eulerian cell containing an interface the unit normal vector to the interface is estimated from the gradient of the colour function F:

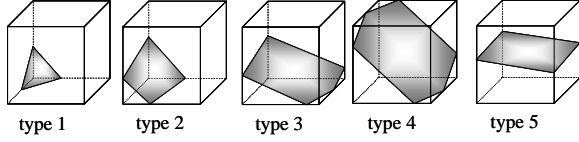$$\overline{n} = \frac{\nabla F}{|\nabla F|} \tag{10}$$

Figure 1: Five generic types of interface configurations considered in the computation of the fluxes through the cell faces.

In our model first the components of the normal vector are computed at the vertices of the Eulerian cell and then the cell-centered components are computed by averaging over the eight surrounding vertices. To minimise the number of possible interface conditions which need to be considered, first a number of transformations at the level of computational cells are carried out to achieve that the components n_1, n_2 and n_3 of the normal to the interface are always positive and satisfy the following inequality:

$$n_1 < n_2 < n_3 \qquad (11)$$

where the subscript refers to the co-ordinate direction. These transformations involve i) change of co-ordinate directions ii) mutual interchange of co-ordinate directions and iii) interchange of the dispersed and continuous phase. Through the use of these transformations it is possible to reduce the total number of possible interface configurations from sixty four to five generic ones which are schematically shown in Fig. 1. From these five generic interface types the particular type prevailing in a certain Eulerian cell needs to be determined on basis of the known interface orientation (i.e. the normal vector to the interface) and the F-value of the interface cell. For the computation of the fluxes through the cell faces the equation for the planar interface segment cutting through the Eulerian cell needs to be considered. This equation is given by:

$$n_1 \xi_1 + n_2 \xi_2 + n_3 \xi_3 = d \qquad (12)$$

where ξ_i $(i = 1..3)$ represents the dimensionless co-ordinate in direction i given by:

$$\xi_i = \frac{x_i}{\Delta x_i} \qquad (13)$$

where Δx_i represents the grid-spacing in co-ordinate direction x_i $(i = 1..3)$. The value of the plane constant d can be determined by equating the expression for the dimensionless liquid volume (volume below the planar interface segments shown in Fig. 1) to the known fractional amount of liquid or the F-value in the interface cell. The value of d can be obtained readily from the root of these non-linear equations using the Newton-Raphson method which needs however to be done with care in order to find the correct root of the cubic equations. As an alternative the Regula Falsi method can be used, which requires however an interval in which the root can be found. This interval can be obtained on basis of the known interface orientation (i.e. components of the normal to the interface) and the fractional amount of liquid in the interface cell (i.e. the F-value) using simple geometrical considerations. One should keep in mind here that the

solution of the non-linear equation needs to be carried out only for the interface cells.

Once the aforementioned steps have been taken, finally the amount of liquid fluxed through each of the faces of the Eulerian cells during a time step Δt can be computed. The F-advection equation is discretised with an explicit treatment of the convections terms, where a straightforward generalisation of the 2D geometrical advection method given by Delnoij (1999) is used (also see Scardovelli and Zaleski, 1999). In our implementation of this method we have adopted the split advection scheme. Because the expressions for the fluxes through the cell faces are quite lengthy they are not given here. Finally the computed new F-values are corrected for (small) non-zero divergence of the velocity field due to the iterative solution of the Pressure Poisson Equation (PPE).

Smoothening of the colour function F

As indicated before the interface orientation (i.e. the normal to the interface) is computed from the gradient of the color function F according to Eq. (8). Basically this involves numerical differentiation of a discontinuous function leading in practice to (small) inaccuracies. This problem can be overcome however by making use of a smoothed color function $\tilde{F}$ for the computation of the unit normal to the interface using Eq. (8) with F replaced by $\tilde{F}$ obtained from:

$$\tilde{F}(\overline{x}) = \sum_m D(x - x_m)D(y - y_m)D(z - z_m)F(\overline{x}_m) \qquad (14)$$

where the smoothening function D is given by the function proposed by Peskin (1977):

$$D(x) = \frac{1}{2h}(1 + \cos(\pi \frac{x}{h})) \qquad (15)$$

or as an alternative by a suitable polynomial expression as the one proposed by Deen et al. (2004b):

$$D(x) = \frac{15}{16} \frac{1}{h} \left[(\frac{x}{h})^4 - 2(\frac{x}{h})^2 + 1 \right] \qquad (16)$$

where h represents the width of the computational stencil used for the smoothening. The summation in Eq. (14) only involves the grid points with distance (in each separate co-ordinate direction) equal or less then the smoothening or filter width h. We typically use h = 2Δ where Δ represents the Eulerian grid size and, unless otherwise stated. The width of the computational stencil for the smoothening should be selected carefully. When the width is too small numerical instabilities may arise, especially in case the coefficient of surface tension is high. On the other hand when the width of the computational stencil is chosen too large, excessive smoothening ("thickening" of the interface) is obtained which is undesirable. For the simulations reported in this paper we used Eq. (16) and additionally we used the smoothed colour function $\tilde{F}$ instead of F in Eq. (8). It should be stressed here that this smoothed colour function is only used in conjunction with the estimation of the unit normal to the interface and not in the computation of the material fluxes through the faces

of the computational cells for which the unsmoothed colour function was used.

Computation of the particle motion and particle-fluid coupling

The equation of motion for the particles is solved with a simple first order integration scheme with linear implicit treatment of the effective drag and added mass forces. Where required the Eulerian quantities such as the liquid phase volume fraction, pressure and velocity components as well as the spatial derivatives of these quantities are interpolated from the staggered Eulerian grid using volume-weighing. The non-ideal particle-particle and particle-wall collisons are taken into account with an event-driven computational scheme using efficient Molecular Dynamics (MD) type of schemes (see Hoomans et al., 1996 and Hoomans, 2000). In the present version of the model we have not accounted for changes in the collision dynamics in case the particles are very close to each other (see Li et al., 1999). The particle-fluid coupling requires Euler-Lagrange and Lagrange-Euler mapping for which we use a volume-weighing technique.

RESULTS

Prior to the presentation of the main results the verification of our computational model will be briefly discussed which involves tests for the flow solver and the two-way coupling of the dispersed phases. For a detailed test of the encounter model we refer to Hoomans et al. (1996) and Hoomans (2000).

Model verification

In our first test the correctness of the implementation of the flow solver was tested for fully developed laminar flow in a square channel with diameter 2a. For this particular case the expression for the fully developed velocity profile can be derived analytically and is given by:

$$v_z = \frac{a^2 \Delta p}{2\mu L} \left\{ 1 - (\frac{x}{a})^2 -4\sum_{n=0}^{n=\infty} \left[\frac{(-1)^n \cos[(n+\frac{1}{2})\pi \frac{x}{a}]}{((n+\frac{1}{2})\pi)^3} \frac{\cosh[(n+\frac{1}{2})\pi \frac{y}{a}]}{\cosh[(n+\frac{1}{2})\pi]} \right] \right\} \quad (17)$$

where the z-coordinate corresponds with the main flow direction. For the simulation the density and viscosity of the fluid were set to respectively 1000 kg/m3 and 1.0 kg/(m.s) whereas the z-velocity at the inlet was set to 1.0 m/s. In Fig. 3 the dimensionless velocity profiles are shown for the central plane cutting through a square duct with diameter 0.02 m obtained from the analytical solution and the solution obtained from the numerical model using 40 computational cells in both the x- and y-direction and 100 cells in the flow direction (duct length 1.0 m). In this figure the average velocity, obtained by integrating Eq. 17 over the cross-sectional area of the column, was used to obtain the dimensionless velocity. As evident from Fig. 2 the agreement between the two solutions is very good with a maximum relative error near the wall of 1.6%. No-slip boundary conditions were used for the walls of the duct
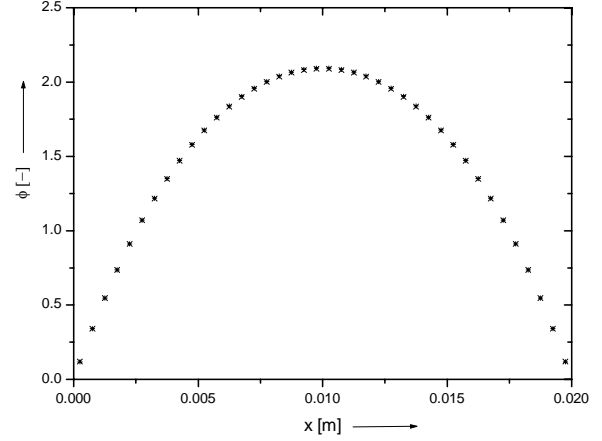

Figure 2: Dimensionless velocity profiles for the central plane cutting through a square duct with diameter 0.02 m obtained from the analytical solution (+) and the numerical solution (x) using 40 computational cells in both the x- and y-direction and 100 cells in the flow direction (duct length 1.0 m).

whereas for the inlet and outlet respectively prescribed (uniform) inflow and prescribed pressure boundary conditions were taken.

In our second test the correctness of the implementation of two-way coupling for the particles was tested by comparing the computed pressure gradient for liquid flow through a fixed bed of particles with the pressure gradient according to the Ergun equation:

$$-\frac{dp}{dz} = 150 \frac{(1-\varepsilon_f)^2}{\varepsilon_f^3} \frac{\mu_l U_0}{d_p^2} + 1.75 \frac{(1-\varepsilon_f)}{\varepsilon_f^3} \frac{\rho_l U_0^2}{d_p} \quad (18)$$

In this test the liquid phase flow field and associated pressure drop was computed for a stationary array of 25x25x125 particles with a diameter of 3.95 mm packed in a square column with a diameter of 0.1 m and a length of 1.0 m. Free-slip boundary conditions were used for the walls of the duct whereas for the inlet and outlet respectively prescribed (uniform) inflow and prescribed pressure boundary conditions were taken. In this case the bed porosity equals 0.495792. The density and viscosity of the fluid were set to respectively 1000 kg/m3 and 0.01 kg/(m.s) whereas the superficial velocity at the inlet was set to 0.1 m/s. For these conditions the pressure gradient according to the Ergun equation equals 20,335 Pa/m. From the numerical model, using 10 computational cells in both the x- and y-direction and 50 cells in the flow direction, an average pressure gradient of 19,273 Pa/m was obtained leading to a relative error of 5.2%. This error can be reduced further by using more computational cells.
Finally van Sint Annaland et al. (2005) performed extensive calculations using their VOF-model for gas bubbles rising in quiescent viscous liquids and demonstrated that the computed terminal rise velocities and shapes of the bubbles agreed very well with those obtained from the Grace diagram (see next section) over a very wide range of Eötvös and Morton numbers, while using a high density and viscosity ratio characteristic for gas-liquid systems. They also showed that i) the size of

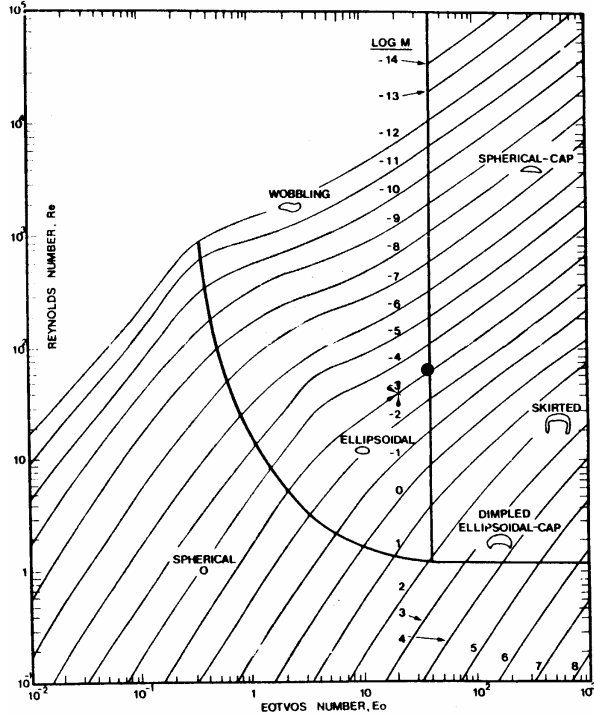the computational domain in the lateral directions should

$$Re_b = \frac{\rho_l v_\infty d_e}{\mu_l} \qquad (21)$$

Figure 3: Bubble diagram of Grace (1973) for the shape and terminal rise velocity of gas bubbles in quiescent viscous liquids.

equal 3 to 4 times the diameter of the bubble to reduce the wall effect to an acceptable level ii) for the gas bubble typically 16 to 20 computational cells (in each direction) are required to correctly predict the bubble characteristics (rise velocity and shape). Van Sint Annaland et al. (2005) also successfully computed the co-axial and oblique coalescence of two bubbles in a viscous liquid, a process which has been studied experimentally by Brereton and Korotney (1991). Clearly the agreement between the computed results and the results obtained from the analytical expressions is very good and therefore our model can be applied with confidence to more complex problems such as gas-liquid-solid systems.

Single gas bubbles

Grace (1973) has analysed a large body of experimental data on shapes and rise velocities of bubbles in quiescent viscous liquids and has shown that this data can be condensed into one diagram, provided that an appropriate set of dimensionless numbers is used. Although this diagram is strictly not valid for gas-liquid-solid systems it is nevertheless useful for reference purposes. A copy of this diagram, taken from Clift et al. (1978) is reproduced in Fig. 3 where the dimensionless Morton (M), Eötvös (Eo) and Reynolds (Re_b) are given by:

$$M = \frac{g \mu_l^4 \Delta\rho}{\rho_l^2 \sigma^3} \qquad (19)$$
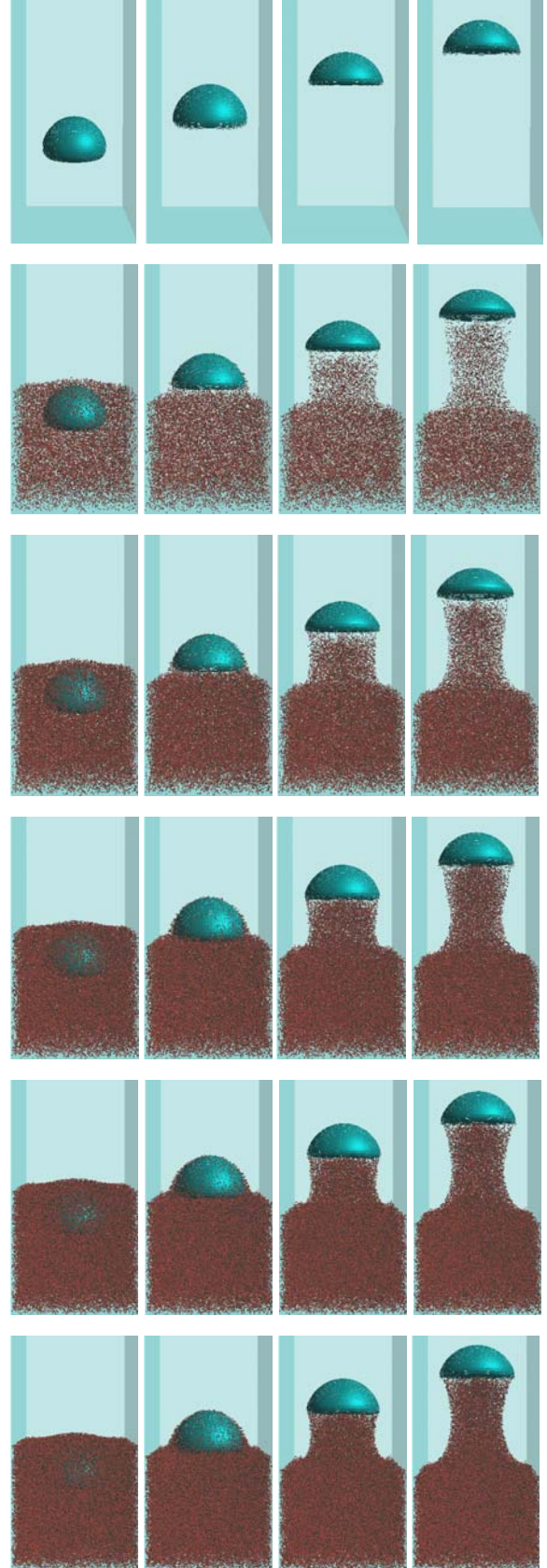
$$Eo = \frac{g \Delta\rho d_e^2}{\sigma} \qquad (20)$$

Figure 4: Rise of a single gas bubble (initial diameter 0.02 m, Eo=38.8, M=9.71.10^{-4}) through a suspension of N_p solid particles (See Table 3 for additional data). For

each series of four frames (from left to right) t=0.05, 0.10, 0.15 and 0.20 s. From top to bottom N_p increases from 0 to 100,000 in these series of frames.

Computational grid	40x40x100 (-)
Grid size	0.001 m
Number of particles	0 (a)
	20,000 (b)
	40,000 (c)
	60,000 (d)
	80,000 (e)
	100,000 (f)
Time step	0.0001 s
Initial bubble radius	0.01 m
Initial bubble position	$(x_0,y_0,z_0) = (0.02, 0.02, 0.02)$ m
Particle density	3000 kg/m^3
Particle diameter	400 μm
Collision parameters e_n, e_t, μ_t	0.9, 0.33, 0.10 (-)
Liquid density	1000 kg/m^3
Liquid viscosity	0.1 kg/(m.s)
Gas density	10 kg/m^3
Gas viscosity	0.001 kg/(m.s)
Surface tension	0.1 N/m

Table 3: Data used for the simulations shown in Fig. 4.

where the effective diameter d_e is defined as the diameter of a spherical bubble with the same volume as the bubble under consideration. In our simulations a fixed density and viscosity ratio of one hundred was used (viscosity and density of the continuous liquid phase equal one hundred times the viscosity and density of the dispersed gas phase).

First the effect of the presence of solid particles on the rise velocity of isolated gas bubbles is assessed. A typical result is presented in Fig. 4, showing the rise of a single gas bubble through a suspension of N_p solid particles. The particles are initially at rest and are randomly distributed over the bottom section of the domain, excluding the volume occupied by the gas bubble. Initially the bubble is spherical and the suspension is quiescent. For all simulations reported in this paper free-slip boundary conditions were applied at the confining walls. The data used for these simulations are given in Table 1. For this particular case the Eötvös and Morton number, based on the physical properties of the pure (i.e. without solid particles) liquid, are respectively equal to 38.8 and $9.71.10^{-4}$, which according to the Grace diagram should correspond to a terminal bubble Reynolds number Re_b of 60. For the pure liquid (i.e. without particles) the computed Re_b equals 46 for all cases and is lower than the value according to the Grace diagram. This discrepancy can be attributed to the relatively small lateral size of the container. For the investigated range of solids volume fraction the retarding effect of the particles on the rise velocity of the bubble is quite small, although small changes in the bubble shape can be discerned. From the series of snapshots given in Fig. 4, the particle drift caused by the rising gas bubble can be clearly seen. While the bubble ascends through the suspension the particles are pushed aside and accumulate at the bubble base.

In Fig. 5 the dimensionless volume of the drift zone X_d is plotted as a function of time for a solids volume fraction $\varepsilon_s=0.0525$ (case f in Table 1). All particles which are present above the initial (horizontal) interface of the

suspension were assigned to the drift zone and from this number of particles N_d the equivalent volume of the
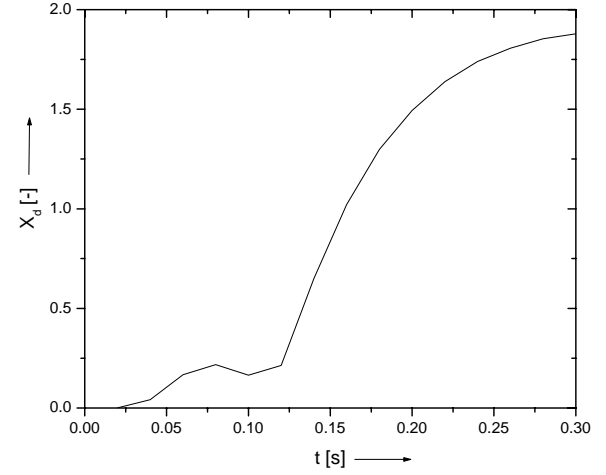

Figure 5: Dimensionless volume X_d of the drift zone behind the rising bubble as a function of time. Total number of particles: 100,000 (case f given in Table 3).

initially uniform suspension was calculated. This volume was finally divided by the bubble volume V_b to obtain the dimensionless volume of the drift zone X_d:

$$X_d = \frac{N_d}{N_p}\frac{V_s}{V_b} \qquad (22)$$

where V_s is the initial volume occupied by the suspension. From this figure it can be seen that this dimensionless volume increases steadily and reaches quite high values (corresponding to twice the bubble volume) indicating appreciable transport of the particles due to the passage of the bubble. In Fig. 6 the dimensionless volume of the drift zone X_d is plotted as a function of the solids volume fraction ε_s (cases b to f in Table 1) 0.30 s after bubble release. Apparently the bubble becomes less effective with respect to the vertical particle transport with increasing solids volume fraction.
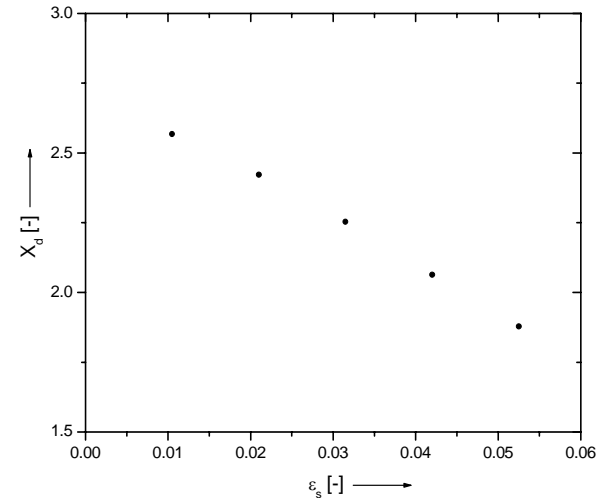

Figure 6: Dimensionless volume X_d of the drift zone as a

function of the solids volume fraction ε_s at t=0.30 s after bubble release.
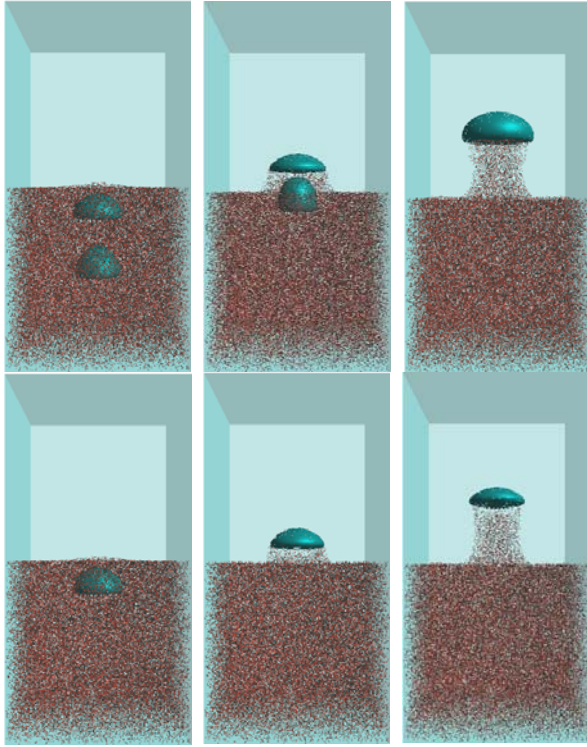

Figure 7: Top: snapshots at different times (t=0.05, 0.10 and 0.15 s) of the co-axial coalescence of two initially spherical bubbles of 0.010 m diameter released from positions (0.020 m, 0.020 m, 0.010 m) and (0.020 m, 0.020 m, 0.025 m) in an initially quiescent liquid in a square column of 0.04 m x 0.04 m x 0.08 m, using a 80x80x160 grid and a time step of 5.10^{-5} s. Eo=16 and M=2.10^{-4}. Bottom: identical calculation with only the leading bubble.

Multiple gas bubbles

The first example involves the co-axial coalescence of two gas bubbles in an initially quiescent suspension where the bubbles are initially spherical with their centres separated by three bubble radii. In Fig. 7 the computed evolution of the bubble shapes is shown before and after the coalescence process. The Morton and Eötvös number for this case are respectively equal to 2.10^{-4} and 16 (based on the individual bubbles) which, according to the Grace diagram, would correspond with a terminal Reynolds number of 50 (case indicated with an asterisk in Fig. 3) which agrees reasonably well with the experimental value of 43 and the computed value of 40. Apparently the leading bubble experiences very little effect of the trailing bubble. However, the behaviour of the trailing bubble is completely different as can be seen clearly from Fig. 7. The trailing bubble catches up with the leading bubble and attains a distinctly different shape than the leading bubble when it enters the wake region of the leading bubble.

The second example involves the oblique coalescence of two gas bubbles in an initially quiescent suspension where the bubbles are initially spherical with their centres separated again by three bubble radii in the vertical direction. Compared to the first case the position of the lower bubble was shifted to the right (x-direction) over 1.6 bubble radii. In Fig. 8 the computed evolution of the bubble shapes is shown before and after the coalescence

process. The Morton and Eötvös number are the same as for the first case. Similar to the previous case the leading
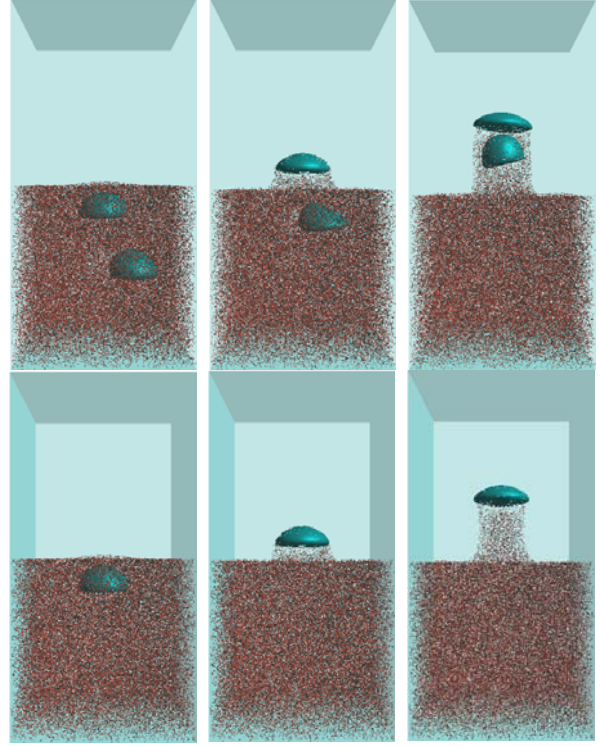

Figure 8: Top: snapshots at different times (t=0.05, 0.10 and 0.15 s) of the oblique coalescence of two initially spherical bubbles of 0.010 m diameter released from positions (0.020 m, 0.020 m, 0.025 m) and (0.028 m, 0.020 m, 0.010 m) in an initially quiescent liquid in a square column of 0.04 m x 0.04 m x 0.08 m, using a 80x80x160 grid and a time step of 5.10^{-5} s. Bottom: identical calculation with only the leading bubble.

bubble behaves as an isolated bubble although its major (vertical) axis attains a small angle with the (vertical) z-axis when the trailing bubble enters its wake region. Again the trailing bubble catches up with the leading bubble and experiences considerable shape deformation when it enters the wake region of the leading bubble.
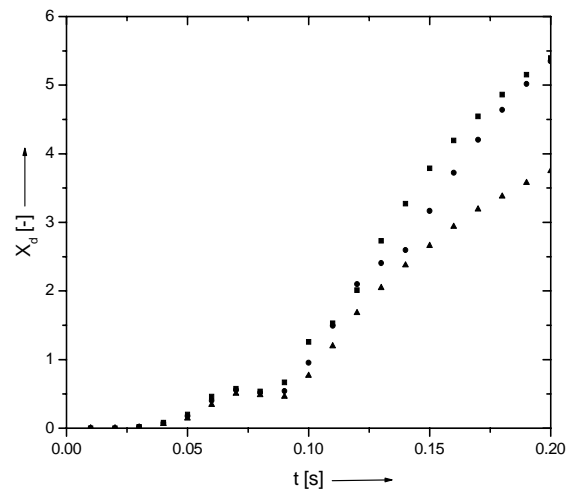

Figure 9: Dimensionless volume X_d of the drift zone behind the rising bubble as a function of time for co-axial bubble coalescence (squares), oblique bubble coalescence

8

(circles) and the case with the leading bubble only (triangles).

In Fig. 9 the results of these two calculations are compared in terms of X_d computed as a function of time. For the purpose of reference the results of the calculation with the leading bubble only are included in this figure. Surprisingly the case with co-axial bubble coalescence leads to the most pronounced vertical particle transport in the bubble wakes.

CONCLUSIONS

In this paper a hybrid model has been presented enabling the direct numerical simulation of gas-liquid-solid flows using a combined Volume of Fluid (VOF) and Discrete Particle (DP) approach applied for respectively dispersed gas bubbles and solid particles present in the continuous liquid phase. The hard sphere DP model, originally developed by Hoomans et al. (1996) for dense gas-solid systems, has been extended to account for all additional forces acting on particles suspended in a viscous liquid and has been combined with the VOF model presented recently by van Sint Annaland et al. (2005) for complex free surface flows.

Our model generates very detailed information on bubble induced particle mixing and can in principle be used to study and quantify the effect of all important physical properties of the gas-liquid-solid system and other variables (such as bubble size and shape) as well. The model has been succesfully applied to compute the particle drift behind rising gas bubbles and revealed that in case multiple bubbles rise, the bubbles compete with each other for the particles drifting behind them.

Clearly computational resources constitute a limiting factor at present. Our model is quite general and it can in principle also be used to study the behaviour of small bubbles (replacing the particles) in the presence of large bubbles provided that appropriate closure equations are used for the (effective) forces acting on the small (unresolved) bubbles.

REFERENCES

BOURLOUTSKI, E. and SOMMERFELD, M. (2002) Transient Euler/Lagrange Calculations of Dense Gas-Liquid-Solid Flows in Bubble Columns with Consideration of Phase Interaction, Proc. 10th Workshop on Two-Phase Flow Predictions, Merseburg, 113-223.

BRACKBILL, J.U., KOTHE, D.B. and ZEMACH, C. (1992). A continuum method for modeling surface tension. J. Comp. Phys. **100**, 335.

BRERETON, G. and KOROTNEY, D. (1991, Coaxial and oblique coalescence of two rising bubbles, AMD-Vol. **119**, Dynamics of Bubbles and Vortices Near a Free Surface. ASME.

BUSSMAN, M., MOSTAGHIMI, J. and CHANDRA, S. (1999). On a three-dimensional volume tracking model of droplet impact. Phys. Fluids, **11**, 1406-1417.

CENTRELLA, J. and WILSON, J. (1984). Planar numerical cosmology. II. The difference equations and numerical tests, Astrophysical J. Suppl. Ser. **54**, 229.

CLIFT, R., GRACE, J.R. and WEBER, M. (1978) Bubbles, Drops and Particles, Academic Press, New York.

DEEN, N.G., VAN DEN HENGEL, E., VAN SINT ANNALAND, M. and KUIPERS, J.A.M. (2004a) Multi-Scale modelling of dispersed gas-liquid two-phase flow, paper no. K07, CD-ROM proceedings of 5th International Conference on Multiphase Flow, ICMF'04, Yokohama, Japan, May 30-June 4, 2004.

DEEN, N.G., VAN SINT ANNALAND, M. and KUIPERS, J.A.M. (2004b). Multi-level modelling of dispersed gas-liquid two-phase flow, Chem. Eng. Sci. **59**, 1853-1861.

DELNOIJ, E. (1999). Fluid dynamics of gas-liquid bubble columns: a theoretical and experimental study, PhD thesis, Twente University, The Netherlands.

DELNOIJ, E., LAMMERS, F.A., KUIPERS, J.A.M. and VAN SWAAIJ, W.P.M. (1997) Dynamic simulation of dispersed gas-liquid two-phase flow using a discrete bubble model, Chem. Eng. Sci. **52**(9), 1429-1458.

GRACE, J.R. (1973) Shapes and velocities of bubbles rising in infinite liquids, Trans. Instn. Chem. Eng., **51**, 116-120.

HIRT, C.W. and NICHOLS, B.D. (1981). Volume of Fluid (VOF) method for the dynamics of free boundaries, J. Comp. Phys. **39**, 201.

HOOMANS, B.P.B, KUIPERS, J.A.M., BRIELS, W.J. and van SWAAIJ, W.P.M. (1996). Discrete particle simulation of bubble and slug formation in a two-dimensional gas-fluidised bed: A hard sphere approach, Chem. Eng. Sci. **51**, 99-108.

HOOMANS, B.P.B, KUIPERS, J.A.M., BRIELS, W.J. and W.P.M. VAN SWAAIJ (1996) Discrete particle simulation of bubble and slug formation in a two-dimensional gas-fluidised bed: A hard sphere approach, Chem. Eng. Sci. **51**, 99-108.

HOOMANS, B.P.B. (2000) Granular dynamics of gas-solid two-phase flows, PhD thesis, Twente University, The Netherlands.

LI, Y., YANG, G.Q., ZHANG, J.P. and FAN, L.S. (2001) Numerical studies of bubble formation dynamics in gas-liquid-solid fluidization at high pressures, Powder Technology. **116**, 246-260.

LI, Y., ZHANG, J. and FAN, L.S. (1999) Numerical simulation of gas-liquid-solid fluidization systems using a combined CFD-VOF-DPM method: bubble wake behavior, Chem. Eng. Sci. **54**, 5101-5107.

LI, Y., ZHANG, J.P. and FAN, L.S. (2000) Discrete phase simulation of single bubble rise behavior at elevated pressures in a bubble column, Chem. Eng. Sci. **55**, 4597-4609.

MITRA-MAJUMDAR, D., FAROUK, B. and SHAH, Y.T. (1997) Hydrodynamic modelling of three-phase flows through a vertical column, Chem. Eng. Sci. **52**(24), 4485-4497.

MITTAL, R. and IACCARINO, G. (2005). Immersed boundary methods, Annu. Rev. Fluid Mech., **37**, 239-261.

NOH, W.F. and WOODWARD, P.R. (1976), SLIC (Simple Line Interface Calculation) method, In : Lecture Notes in Physics, A.I. van de Vooren and P.J. Zandbergen (eds.), 330.

PESKIN, C.S. (1977). Numerical analysis of blood flow in the heart, J. Comp. Phys., **25**, 220-252.

POPINET, S. and ZALESKI, S. (1999). A front-tracking algorithm for accurate representation of surface tension. Int J. Numer. Meth. Fluids, **30**, 775-793.

PROSPERETTI, A. (2001), Navier-Stokes numerical algorithms for free-surface flow computations : An overview. Drop Surface Interactions, 21.

RIDER, W.J. and KOTHE, D.B. (1998). Reconstructing volume tracking, J. Comp. Phys., **141**, 112-152.

RUDMAN, M. (1997). Volume-tracking methods for interfacial flow calculations, Int. J. Num. Methods in Fluids, **24**, 671-691.

RUDMAN, M. (1998). A volume-tracking method for incompressible multifluid flows with large density variations. Int. J. Num. Methods in Fluids, **28**, 357-378.

SCARDOVELLI, S. and ZALESKI, S. (1999). Direct numerical simulation of free-surface and interfacial flow, Annu. Rev. Fluid Dyn., **31**, 567-603.

VAN DER HOEF, M.A., BEETSTRA, R. and KUIPERS, J.A.M. (2005) Lattice Boltzmann simulations of low Reynolds number flow past mono- and bidisperse arrays of spheres: results for the permeability and drag force, J. Fluid Mech., **528**, 233-253.

VAN DER HOEF, M.A., VAN SINT ANNALAND, M. and KUIPERS, J.A.M. (2004). Computational fluid dynamics for dense gas-solid fluidized beds: a multi-scale modeling strategy, Chem. Eng. Sci., **59**, 5157-5165.

VAN SINT ANNALAND, M., DEEN, N.G. and KUIPERS, J.A.M. (2003) In: Sommerfeld, M. and Mewes, D. (eds.), Multi-level modelling of dispersed gas-liquid two-phase flows, series: Heat and Mass Transfer, Springer. Springer, Berlin.

VAN SINT ANNALAND, M., DEEN, N.G. and KUIPERS, J.A.M. (2005) Numerical simulation of gas bubbles behaviour using a three-dimensional volume of fluid method, Chem. Eng. Sci., **60**, 2999-3011.

YOUNGS, D.L. (1982). Time-dependent multi-material flow with large fluid distortion, In: Numerical methods for fluid dynamics, K.W. Morton and M.J. Bianes (Eds.), Academic Press, New York, 273-285.

ZHANG, J.P., LI, Y. and FAN, L.S. (2000a) Numerical studies of bubble and particle dynamics in a three-phase fluidized bed at elevated pressure, Powder Technology. **112**, 46-56.

ZHANG, J.P., LI, Y. and FAN, L.S. (2000b) Discrete phase simulation of gas-liquid-solid fluidization systems: single bubble rising behavior, Powder Technology. **113**, 310-326.